Filamentation Instabilities in

Relativistic Plasmas

Thesis submitted in partial fulfillment of the requirement for the degree of master of science in the Faculty of Natural Sciences

Submitted by: Almog Yalinewich

Adviser: Prof. Michael Gedalin

Department of Physics

Faculty of Natural Science

Ben-Gurion University of the Negev

July, 2008

Abstract

In this work we calculate the growth rates of plasma instabilities that occur in counter - streaming plasma, during the linear stage. Although our formalism can detect several kinds of instabilities, we are particularly interested in instabilities that cause current filamentation and generates magnetic fields. Such instabilities plasy a key role in particle acceleration in collisionless shocks and generation of powerful magnetic fields in astrophysical phenomena. Most of these phenomena are currently not fully understood, so a detailed study of the instabilities may shed light on some of them. Also, the Fast Ignition Scheme for Interial Confinement Fusionm, where deutrium - tritium plasma is ignited by an electron beam, is susceptible to such instabilities. When they occur, they tend to disperse the energy and thwart thermonuclear ignition. Thus, a better understand of the instabilities can improve the design of FIS systems.

In this work we will focus on instabilities that arise in GRB afterglows. Current theory suggests that the instability erupts when ultrarelativistic jets emitted from the explosion of the GRB progenitor collide with interstellar plasma. The evolution of the system can be divided into two stages. In the first stage, only the

electrons respond to the instability, because they are much lighter than protons. In the second stage, the protons begin to respond to the instability, but by that time the electrons have already reached thermal equilibrium.

The first stage has been thoroughly studied in the past few decades, both experimentally and theoretically. The second stage, however, is less understood, mainly due to the fact it involves two species with large mass ratio (which means that the problem contains two very different time scales).

As was mentioned before, we study only the linear stage of the instabilities. One must be careful when drawing conclusions from the linear stage, due to nonlinear effects which may alter some properties of the instability. One example is the thickness current filaments, which differs from the wavelength of the dominant mode because the filament tend to coalesce after the linear stage. However, some properties are preserved even in the nonlinear stage, like the direction of the wavenumber of the dominant mode, which determines the pattern of the filaments.

We show that the best condition for magnetic field generation is a

symmetric collision. When the collision is asymmetric, When the asymmetry is large enough, the dominant mode becomes electrostatic and no magnetic fields are generated. However, the second stage can still generate magnetic fields, even in the case of an asymmetric collision.

Moreover, the results can be used to direct the attention of computer simulations to the relevant areas in parameter space. Plasma simulations track trajectories of millions of particles, so even simple calculations pose a daunting computational task for modern computes. In order to reduce run times, programmers make simplifying assumptions on the directions of the electromagnetic fields, the wavevector of the instability. Others run simulations with lower electron - proton mass ratio. Obviously, making a wrong assumption will cause the simulation to return wrong results. Therefore, the results of this work can be used to verify assumptions made in the past, and help choose the assumptions to be used in the future.

Contents

1 Introduction

1.1 plasma instabilities

According to the equipartition theorem [1], in a state of equilibrium, the total energy divides equally between all degrees of freedom. A corollary of that law is that in the absence of external forces, the equilibrium momentum distribution of an ensemble of particles is isotropic. Hence, a system of particles with anisotropic distribution function is unstable, and tends to relax into an isotropic distribution with the same energy and momentum. In non ionized fluids, equilibrium is attained by collisions between molecules. Plasmas can also reach equilibrium through processes called plama instabilities. Plasma instabilities cause rapid growth of long range electromagnetic fields (in contrast to the short range fields in the case of collisions). Collisions and plasma instabilities are competing relaxation processes, so the latter occurs only in collisionless plasmas, i.e. plasmas so tenuous that collisions seldom occur.

A system of two beams of counter - streaming, collisionless

plasmas gives rise to several types of plasma instabilities. These instabilities differ by the direction of the electric field, and the direction in which it varies. Authors distinguish three major types of instabilities:

1.1.1 Two stream instability

Bohm and Gross [2] discovered an unstable mode that attacks counter - streaming plasmas, in which the growing electric field points parallel to the beam, and oscillates in that direction. Buneman [3] extended the analysis to take into account beams of composed of different particles (such instability is often referred to as the Buneman instability). Since all the variables vary and point along the same direction, this instability is the simplest to analyse and simulate by a computer programme. This instability is said to be electrostatic because the wavenumber and the electric field are aligned. According to Faraday's law in k space representation

$$\mathbf{k} \times \mathbf{E} = \frac{\omega}{c}\mathbf{B} \tag{1}$$

one can see that this instability does not generate magnetic fields. In order to understand this instability on a microscopic level, one has to consider a beam of cold particles moving in the presence of a spatially oscillating electric potential. The potential profile in this case resembles an alternating pattern of hills and troughs. Particles slow down when they climb up a potential hill, and accelerate when they tubmle into a trough. Therefore, the charge density near hills should increase, while the charge density near troughs should decrease. Such charge distribution would generate an electric field that reinforces the initial perturbation, and this closes the feedback loop. Obviously, this instability cannot grow indefinitely, so at some point another mechanism must kick in and stop the instability. This is called saturation. The saturation mechanism in the two stream instability is particle trapping in potential troughs; when the peak of the electric potential is greater than the kinetic energy of the particles, then they become trapped between two adjacent peaks and the instability stops [7].

1.1.2 Weibel instability

Weibel [4] and Fried [5] discovered a mode in which the growing electric field points in the direction of the beam, but varies perpendicular to the beam. This instability is said to be electromagnetic because the electric field is perpendicular to the wavenumber, so according to Faraday's law 1, magnetic field generation is maximal, for a given length of **E**,**k**. In order to understand this instability on a microscopic level, one has to consider two beams of charged particles moving parallel and anti parallel to the z axis (see figure 1). Suppose now that we add a small magnetic field $b\hat{x}\cos(ky)$ (i.e. points along the x axis, and varies along the y axis). Particles moving in the positive z direction will be scattered away from the odd nodes, and concentrate around the even nodes, while particles moving in the negative z direction will be scattered away from even nodes, and concentrate around the odd nodes. As a result, there will be a nonzero net current near nodes. The current will induce a magnetic field that will reinforce the initial disturbance, and that, in turn will amplify the current and so

on [25]. The instability generates electromagnetic fields and creates current filaments [26]. This is the reason why the Weibel instabilty is sometimes called filamentation instability. The saturation mechanism in the Weibel instability is magnetic trapping of particles in filaments [8]; when the magnetic fields are so strong that the Larmor radius becomes smaller than the thickness of the filament, particles entering the filament will move in closed orbits. A more detailed study of the saturation mechanisms is given in [19]. Another phenomenon that occurs during saturation is the coalescence of current filaments [9], due to the fact that like currents attract and opposite repel each other [18,19]. This means that the initial wavelength of the disturbance may be different from the final wavelength of the filaments.

1.1.3 Oblique instability

Bludman, Watson and Rosenbluth [6] have shown that in some cases the dominant instability might be of a third type: an oblique mode, where the electric field points and varies in acute angles to

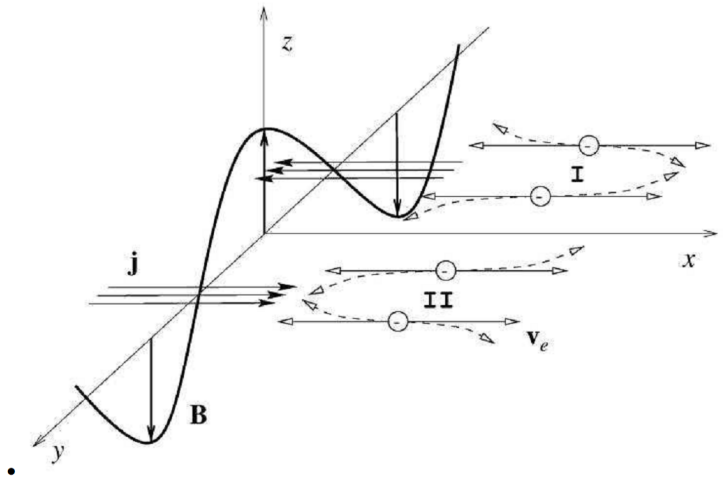

Figure 1: Sinudoidal curve describes intensity of the magnetic field. The horizontal arrows describe the original direction direction of the charged beams. The dashed lines describe the direction under the influence of the magnetic field (taken from ref [25])

the beam. This instability is the hardest to analyse, and therefore very little is known about it. It recieved attention only recently [42,43] due to its possible role in the Fast Ignition Scheme for Interial Confinement Fusion.

The density patterns that form during each of the three instabilities are shown in figure 2.The Weibel instability creates current

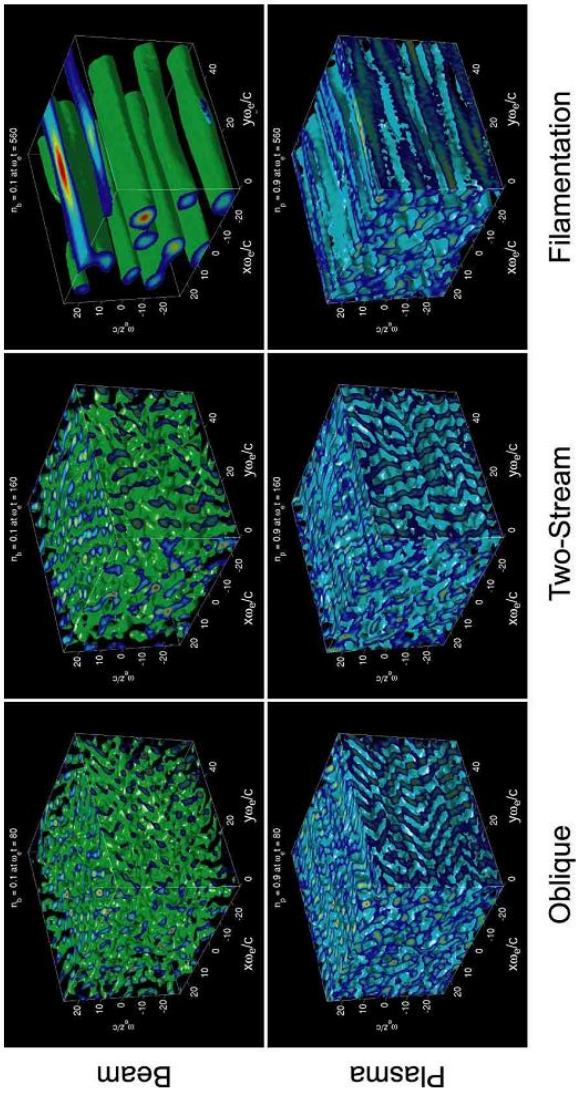

Figure 2: Simulations preformed in [33] demonstrate the particle density patterns that form during each of the instabilities. In the Filementation instability, the particles concentrate in pipe-like structures paralell to the direction of the flow. In the two stream instability, the particles concentrate in planes perpendicular to the direction of the flow. In the oblique instability, the particles concentrate in a zig zag pattern. Original flow direction is along the y axis.

filaments parallel to the direction of the original beam. In the two stream instability, the density varies only along the original direction of motion, so the particles concentrate in sheets perpendicular to the beam. In the oblique instability the electric field and the wavevector are at an acute angle to the beam, so the particles tend to concentrate in a zig zag pattern, such that every linear section is at an obtuse angle to the beam.

This document focuses on the initial stage of the instabilities. In the initial stage, each mode grows exponentially with time, independent of the other modes. In this stage, the equations are greatly simplified by the assumption that the unstable modes are very small, so we can use perturbation theory (see below). However, finding the unstable spectrum in the general case poses a daunting task. Many previous calculations were mitigated by simplifying assumptions on the direction of the electric field, the direction in which it varies, the particle distribution function and density ratio [10, 11,12]. In this document we will find the unstable spectrum without mitigating assumptions, and use this solution to analyse plasma instabilities that occur in astrophysics.

1.2 Particle in Cell simulations

A computer could, in principle, follow the trajectory of each particle and compute the force due to the others. However, since it has to cycle through all pairs, the complexity of such algorithm would be $O\left(n^2\right)$ (where n is the number of particles). Since this algorithm turned out to be too slow to be practical, a faster algorithm, the Particle In Cell method, was developed.

In the PIC method, space is divided into a discrete grid, and the average charge density and current are evaluated at each vertex. Afterwards, The fields are expanded in Fourier series, and the programme solves Maxwell's equation for the coefficients. Finally, the programme solves the equation of motion for the velocities and advances the particles in time and space.

The complexity of such algorithm is $O\left(n\right)$, but the discrete grid introduces numerical artifacts to the results. One of the these artifacts is aliasing, which occurs because the distance between particles is smaller than the cell size. Another is the Courant -

Friedrich restriction

$$k\,c\,\Delta t < 2 \tag{2}$$

Where k is the wavenumber, c is the speed of light and Δt is the time step. When this condition is violated, the algorithm becomes numerically unstable. This means that the time step limits the maximum k of the modes the programme can reliably simulate.

Another difficulty in PIC simulations arises when considering multispecies plasma, escpecially when the particle mass ratio is large (as in electron - proton plasma). Each species introduces its own timescale to the problem (namely, the inverse of the plasma frequency). The time step is determined by the timescale of the lighter species, while the relaxation processes can take as long as dozen time scales of the heavier species [22]. Because of these constraints, a 3D simulation of electron - proton plasma is currently too intensive to be practical. Instead, simulations either examine two species plasma with smaller mass ratio [23] or with less dimensions [22],[30].

We presented here a brief description of the PIC method. A more

detailed discussion is given in [24]

2 Motivation

In this section we will describe two physical phenomena in which plasma instabilities play a key role. The purpose of this section is to elucidate the motivation for studying these instabilities. The two phenomena are GRB afterglow in astrophysics, and the second is the Fast Ignition Scheme in Inertial Confinement fusion. In the first, the Weibel instability is an essential ingredient, while in the latter it is an undesired side effect. Although we will later on focus solely on the astrophysical context, we wish to mention the other application in order to show that this discussion may also have a practical use.

2.1 Astrophysics

Gamma ray bursts are intense flashes of gamma radiation from outer space that last for a fraction of a second. They have been extensively studied since their serendipitous discovery in 1967 [13]. They are believed to be caused by powerful explosions [14] (the entity that explodes when a GRB occurs is referred to as its pro-

genitor) that accelerate particles to $\gamma \sim 10^2 - 10^3$ [31,32] (γ being the Lorentz factor).

Some GRBs are followed by a longer wavelength, longer lived, decaying afterglow. According to a model proposed in [15], GRB afterglow radiation eminates from ultrarelativistic electrons which meander in a magnetic field. They distinguish two types of radiation. The first is synchrotron radiation [16]. This radiation emerges from particles which move in a helical trajectory in a constant magnetic field, or at least, varies on a length scale much larger than the Larmor radius. The second kind is jitter radiation [17]. This radiation emerges from particles meandering in a spatially oscillating magnetic field. This model assumes the magnetic field changes on a length scale much smaller than the Larmor radius, so each particle experiences many random small angle deflection during its flight, so on average it keeps moving in its original trajectory.

These two types of radiation are in fact two extreme cases of the same problem, namely, motion of a charged partilce in a magnetic field. Synchrotron radiation corresponds to the assumption that

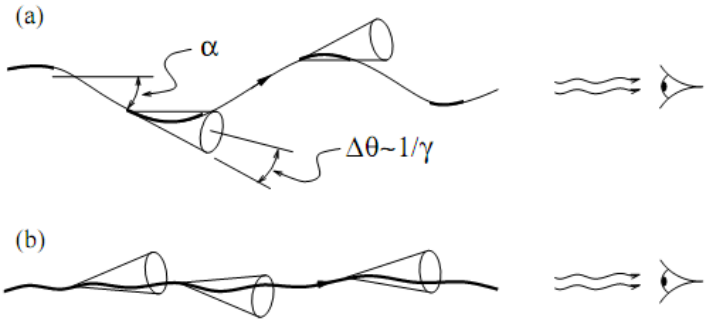

FIG. 1.—Emission from various points along the particle's trajectory. (*a*) $\alpha \gg \Delta\theta$; emission from selected parts (*bold portions*) of the trajectory is seen by an observer. (*b*) $\alpha \ll \Delta\theta$; emission from the entire trajectory is observed.

Figure 3: The trajectory and beaming angle in synchrotron and jitter radiation (taken from [15])

the beaming angle is much smaller than the deflection angle, and jitter radiation to the assumption that the beaming angle is much larger than the deflection angle (see figure 3). It has been shown that a combination of synchrotron and jitter radiation fits the spectrum of a GRB afterglow [15] (see figure 4).

Over the years, several possible mechanisms for magnetic field generation were examined, but they all turned out to be wither too weak or too slow, except the Weibel instability [25]. We believe today that the Weibel instability is responsible for the magnetic field required for jitter and synchrotron radiation in GRB after-

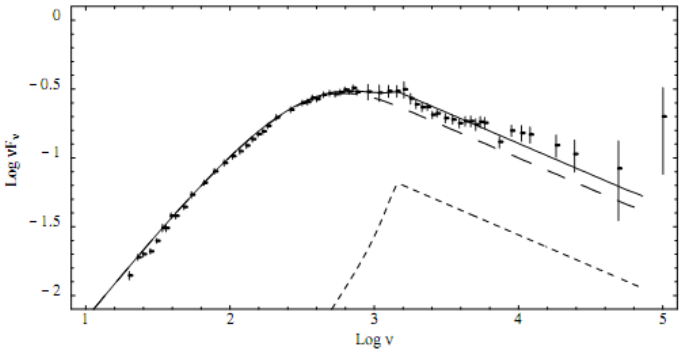

FIG. 11.—Visual fit of a spectral shape for GRB 910503. The inferred values are $B_0^2/B_{SS}^2 = 7$, $\delta = 0.07$, $\mu = 10$, and $p = 3.9$. The synchrotron (*long-dashed curve*) and jitter (*short-dashed curve*) spectral subcomponents are also shown.

Figure 4: Comparison of the theoretical and measured afterglow spectrum (taken from [15])

glows.

The contemporary model for GRB afterglow can be summarised as follows:

1. The progenitor explodes
2. Dense relativistic jets shoot out
3. The jet collides with interstellar plasma
4. Plasma particles reflect from the jet front
5. In the jet frame, particles that haven't yet collided with the jet move toward it, while those that have collided with it move away from it. Thus, a counter - streaming profile is formed

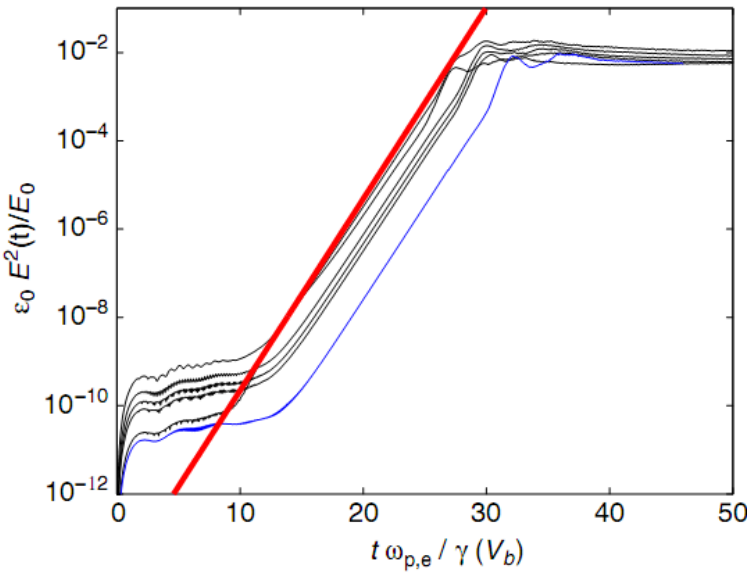

Figure 5: Electrostatic energy as a function of time. First rise is due to electron instability, and second rise due to proton instability. Taken from [22]

6. The Weibel instability developes. At early times, only the electrons respond to it because they are much lighter than protons.

7. The electrons reach a state of thermal equilibirum

8. The protons begin to respond to the instability, in the presence of the thermalised electron background [18,19]. (see figure 5).

9. Magnetic fields are generated

10. Particles scatter from the magnetic field and emit radiation

One of the standing questions regarding these instabilities is whether the dominant mode (that which grows fastest in the linear stage) occurs when the wave vector is perpendicular or oblique to the beams (if the wave vector is parallel to the beam, then the two stream instability occurs, and it is of no interest to us in this context because it does not generate magnetic fields). Many authors ([20] for example) assumed that the dominant mode is perpendicular to the beam. Later on, we will check whether (or more precise, under what conditions) this assumption is valid.

2.2 Fast Ignition Scenario for Inertial Confinement Fusion

The purpose of ICF is to ignite and control thermonuclear burn. In 1994, Tabak et al [21] proposed an ignition technique called "Fast Ignition Scheme". Their idea is illustrated in figure 6

The initial configuration is a fuel pellet impaled on a gold cone. At first, the laser beams irrdiate the outer shell of the pellet and compresses the interior by thermal ablation. When the the pellet

Figure 6: Three stages of FIS (left to right): Lser irradiation, ablative compression and heating by an electron beam

reaches a certain density, another laser beam is fired into the gold cone, which causes the gold atoms to eject a beam of electrons into the fuel pellet. The electron beam heats up the fuel, and thermonuclear burn begins. One of the difficulties in this scheme is that during the stage when the electron beam from the gold cone interact with the plasma inside the fuel pellet, plasma instabilities might develope. Those instabilities tend to disperse the energy and lower the burn efficiency. Hence, a better understanding of those instabilities might help improve the FIS design.

3 Methodology

In this section we will present the governing equations that determine the time evolution of plasmas. Then, we will present two ways by which these equations are analysed, and comment on their advantages and disadvantes, overlap, and the ways they complement each other.

3.1 Governing equations

Since the phenomenon we study are electromagnetic in nature, so the governing equatiosn must include Maxwell equations: Faraday's law

$$\nabla \times \mathbf{E} = -\frac{1}{c}\frac{\partial \mathbf{B}}{\partial t} \tag{3}$$

Ampère's law

$$\nabla \times \mathbf{B} = \frac{1}{c}\frac{\partial \mathbf{E}}{\partial t} + \frac{4\pi}{c}\mathbf{J} \tag{4}$$

We also assume that there are no collisions, so the particle dy-

namics are determined by the collisionless Boltzmann equation

$$\frac{\partial f_\sigma}{\partial t} + \mathbf{v} \cdot \frac{\partial f_\sigma}{\partial \mathbf{r}} + q \left[\mathbf{E} + \frac{\mathbf{v}}{c} \times \mathbf{B} \right] \frac{\partial f_\sigma}{\partial \mathbf{p}} = 0 \tag{5}$$

Which is sometimes called the Vlasov equation. σ in eq. 5 denotes species index. According to this equations, there is no direct interaction between particles, but only the interaction of particles with the field. Notice we omitted two of Maxwell's equations, namely, Gauss's laws for the electric and magnetic fields

$$\nabla \cdot \mathbf{E} = 4\pi\rho \tag{6}$$

$$\nabla \cdot \mathbf{B} = 0 \tag{7}$$

The reason is that the Gauss laws can be derived from the other two Maxwell equations and charge conservation. Since charge conservation is already included in the Vlasov equation (it is the first moment of eq. 5), the Gauss laws are redundant.

The last relation that is required to close this set of equations is

the definition of current

$$\mathbf{J} = \sum_{\sigma} \int f_{\sigma} \mathbf{v} d^3 p \tag{8}$$

3.2 Linear stability analysis

We assume some initial distribution functions $f_{\sigma}^{0}(\mathbf{p})$, and that the initial electromagnetic fields are zero. Next, we add small disturbances that vary as $\exp(i\mathbf{k} \cdot \mathbf{r} - i\omega t)$. Every derivative turns into a multiplication by a constant: $\frac{\partial}{\partial t} \rightarrow -i\omega$, $\frac{\partial}{\partial \mathbf{r}} \rightarrow i\mathbf{k}$, and the differential equation turns into an algebric equation. After some algebra, we arrive at

$$\left[\frac{\omega^2}{c^2} \varepsilon(\mathbf{k}, \omega) + \mathbf{k} \otimes \mathbf{k} - k^2 \mathbf{I} \right] \mathbf{E}_{\mathbf{k}} = 0 \tag{9}$$

Where $\otimes$ denotes tensor product, and the dielectric tensor is given by

$$\varepsilon\left(\mathbf{k},\omega\right)=\mathbf{I}+\frac{4\pi q^2}{\omega}\int d^3p\frac{\mathbf{v}}{\omega-\mathbf{k}\cdot\mathbf{v}}\frac{\partial f}{\partial\mathbf{p}}\cdot\left[\left(1-\frac{\mathbf{k}\cdot\mathbf{v}}{\omega}\right)\mathbf{I}+\frac{\mathbf{k}\otimes\mathbf{v}}{\omega}\right] \tag{10}$$

$$\varepsilon_{\alpha\beta}\left(\mathbf{k},\omega\right)=\delta_{\alpha\beta}+\sum_\sigma\frac{\omega_{p\sigma}^2}{n\omega^2}\int\frac{p_\alpha}{\gamma}\frac{\partial f_\sigma^0}{\partial p_\beta}d^3p+\sum_\sigma\frac{\omega_{p\sigma}^2}{n\omega^2}\int\frac{p_\alpha p_\beta}{\gamma}\frac{\mathbf{k}\cdot\partial f_\sigma^0/\partial\mathbf{p}}{m\omega\gamma-\mathbf{k}\cdot\mathbf{p}} \tag{11}$$

Equation (9) has the form $\mathbf{T}\cdot\mathbf{E}_\mathbf{k}=0$. Nontrivial solutions ($\mathbf{E}_\mathbf{k}\neq\mathbf{0}$) exist if $|\mathbf{T}|=0$, and that yields the dispersion equation. Without restriction to generality, we assume $\mathbf{k}=(k_x,0,k_z)$ and that f is an even function of p_x,p_y (hence $\varepsilon_{xy}=\varepsilon_{yz}=0$), so the dispersion equation takes the form

$$\left(\frac{\omega^2}{c^2}\varepsilon_{yy}-k^2\right)\left[\left(\frac{\omega^2}{c^2}\varepsilon_{xx}-k_z^2\right)\left(\frac{\omega^2}{c^2}\varepsilon_{zz}-k_x^2\right)-\left(\frac{\omega^2}{c^2}\varepsilon_{xz}+k_zk_x\right)^2\right]=0 \tag{12}$$

A more detailed derivation is given in [11]. The first branch of the dispersion equation yields only stable modes or modes with relatively small growth rate [18], and will be disregarded henceforth. What remains is to solve the dispersion equation for ω.

After we solve the dispersion equation, we can find the directions of the growing electromagnetic fields. We solve the degenerate system of linear equations

$$\mathbf{T}\cdot\mathbf{E}_{\mathbf{k}}=\begin{bmatrix}\varepsilon_{xx}-\frac{k_z^2c^2}{\omega^2} & 0 & \varepsilon_{xz}+\frac{k_xk_zc^2}{\omega^2}\\ 0 & \varepsilon_{yy}-\frac{k^2c^2}{\omega^2} & 0\\ \varepsilon_{xz}+\frac{k_xk_zc^2}{\omega^2} & 0 & \varepsilon_{zz}-\frac{k_x^2c^2}{\omega^2}\end{bmatrix}\begin{bmatrix}E_{\mathbf{k}x}\\ E_{\mathbf{k}y}\\ E_{\mathbf{k}z}\end{bmatrix}=0 \tag{13}$$

Since we disregard the first branch, we can set $E_{\mathbf{k}y}=0$. The direction of the electric field in the xz plane is determined by the ratio of the two nonzero vector components

$$\frac{E_{\mathbf{k}x}}{E_{\mathbf{k}z}}=-\frac{\omega^2\varepsilon_{zz}-k_x^2c^2}{\omega^2\varepsilon_{xz}+k_xk_zc^2}=-\frac{\omega^2\varepsilon_{xz}+k_xk_zc^2}{\omega^2\varepsilon_{xx}-k_z^2c^2} \tag{14}$$

Or, alternatively, by the ratio of the components parallel and perpendicular to the k vector

$$\frac{E_{\mathbf{k}\perp}}{E_{\mathbf{k}\parallel}}=\frac{(E_{\mathbf{k}x}/E_{\mathbf{k}z})\cos\theta_{\mathbf{k}}-\sin\theta_{\mathbf{k}}}{(E_{\mathbf{k}x}/E_{\mathbf{k}z})\sin\theta_{\mathbf{k}}+\cos\theta_{\mathbf{k}}} \tag{15}$$

Where $\cos\theta_{\mathbf{k}}=\frac{k_z}{\sqrt{k_x^2+k_z^2}}$. According to Faraday's law, $\mathbf{B}_{\mathbf{k}}\propto\mathbf{k}\times\mathbf{E}_{\mathbf{k}}$. Since Both $\mathbf{k},\mathbf{B}_{\mathbf{k}}$ lie in the xz plane, $\mathbf{B}$ always points in the

y direction.

Full derivation of the equations developed in this section is given in [11].

3.3 Solution of the dispersion equation

Equation 12 is often transcendental, so a numerical solution must be employed. We tested several popular numerical methods, namely, Newton - Raphson, Brent's method and Bisection [29]. We soon realised that these methods were of no avail due to their reliance on a good initial guess (finding a good initial guess is tantamount to solving the dispersion equation). Moreover, the number of iterations required for these algorithms is unbounded, and they often failed to converge. We therefore resorted to a more primitive, bruteforce and surefire method, that, although lacking the elegance of the previous methods, proved much more efficient in root finding. We will elaborate on this 'Brute force' method momentarily.

We recall that the dispersion equation is complex, so it can be

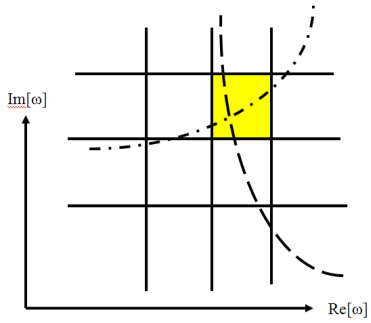

Figure 7: Root finding algorithm. The solid lines represent the grid lines in . The dashed line represents the contour along which the real part of the dispersion equation is zero, and the dash dot line represents the contour along which the imaginary part of the dispersion equation is zero. The yellow square is that which the algorithm registers as containing a square.

decomposed into two real equations. Hence, the solution is also comprised of two real components. The algorithm begins with a rectengular area that should contain the root. The algorithm proceeds by dividing the area into many smaller squares, and sweeps over all the smaller squares in search of a root. The algorithm detects a root by going over all the sides to check whether the one of the components of the dispersion equation has different signs on different vertices. If both components change signs along the sides of the same square, then the data of that square is registered. The algorithm is demonstrated in figure [7].

The brute force method has two prominent advantages. First, the number of iterations is bounded. The maximum number of evaluations equals the number of vertices on the grid. If we are interested only in the fastest growing mode, we can start sweeping the grid from the top, and stop sweeping as soon as we come across a root. Second, It does not require an initial guess.

However, this method has also many disadvantages, of which we will survey the most pronounced:

1. Long execution time. If the grid has n points along each axis, then in the worst case, the algorithm will require n^2 evaluations of the dispersion equation. The algorithm is therefore said to be of complexity $O\left(n^2\right)$.
2. The precision of the results is bounded by the cell size. The algorithm only identifies squares that contain a root. The uncertainty in the location of the root is therefore equal to the dimensions of the square. This drawback can be mitigated by either applying the algorithm recursively to the area bound by the square, or feeding the centre of the square as a first guess to one of the algorithms previously disqualified. We were content with the precision obtained from an unrefined calculation, so we used neither method.
3. False positive and true negative identifications. When the grid is too coarse the algorithm might either register a square

that does not encompasses a root (false positive) or miss a squre that does encompass a root.(true negative). The two caes are illustrated in fig 8. Both should disappear when the grid is refined.

4. Requires proper choice of the boundaries for the initial region in ω space. On the one hand, the region should be large enough to ensure that it contains the root, but on the other hand, if the region is too big then either the execution time becomes too long (if the resolutions is preserved) or the grid becomes too coarse and the precision decreases (if the number of points is preserved). A proper choice of the size of the region should optimize this tradeoff, and we usually attain it by trial and error. A propery of the dispersion equation that comes to our aid in this consideration is the asymptotic stability. For any physical initial distribution function, the dispersion equation 12 can be shown to reduce to the vacuum dispersion equation

$$\omega^2 - c^2 k^2 = 0 \tag{16}$$

When the limit $|\omega| \to \infty$ is taken [27]. The physical interpretation of this limit is that when the field changes too fast, then the particles hardly deviate from their original position, meaning they do not respond to the fields, so the latter evolves as if there were no particles at all.

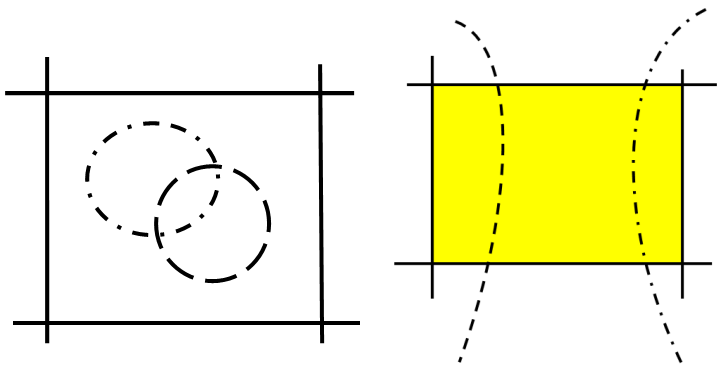

Figure 8: True negativ (on the left) and false positive (on the right). As in fig 7, solid lines represent grid lines, dashed and dash dot lines represent contours along which the real and imaginary parts of the dispersion equation are zero, and a yellow square means that it has been identified by the algorithm as encompassing a root. In the true negative case, the contours intersect, so the square encompasses two roots, but none of the contours intersect the grid lines, so the algorithm doesn't register this square. In the false positive case, both contours intersect the grid lines, but not one another. Therefore, the algorithm registers this square, but it does not encompass a real root.

4 Numerical Analysis

4.1 Immobile background

In this section we analyse simple systems in which plasma instabilities can erupt. They are simple in the sense that they are characterised by a small number of parameters, are easily solved, and their results can be readily interpreted. The purpose of these exercises is to help us understand the relation between the initial conditions and the properties of the resulting instabilities, and also, these exercises will serve as benchmarks for more complicated models. These calculations can also be applied to the first stage of the instability in afterglows, where only the electrons participate. We will begin with the simplest case (cold beams of equal densities) and then we will introduce finite temperature and density variation in order to study their effects on the instability.

4.1.1 Cold beams of equal densities

We consider two beams of electrons flowing parallel and anti parallel to the z axis. We assume that each electron moves with the mean velocty its beam, and that there exists a charge neutralizing background of stationary protons. The corresponding distribution function of the electrons is

$$f(\mathbf{p}) = \frac{n}{2}\delta(p_x)\,\delta(p_y)\,[\delta(p_z - P) + \delta(p_z + P)] \qquad (17)$$

This is the simplest case in which the Weibel instability occurs. It is characterised by a single parameter, P, which is the magnitude of the momentum of each particle prior to the instability. The resulting dispersion equation for this distribution function is bi quartic in the frequency, so there exists an analytic, closed form solution. Due to the length of the expressions involved, the full dispersion equation will be given in the appendix. Here we give key features of this system and display numerical results for a single case which is of interest in regard to GRB afterglows. In presenting the results we use the following dimensionless vari-

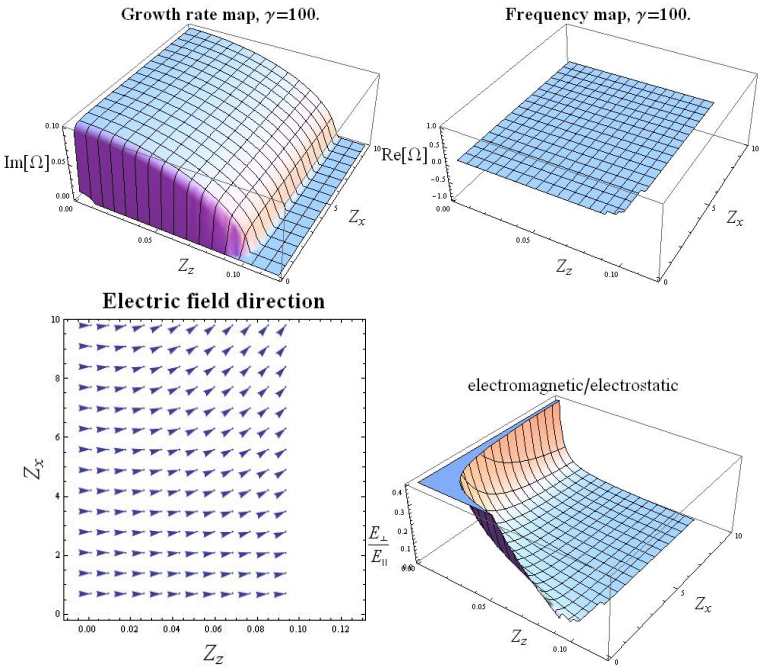

Figure 9: Imaginary part of the frequency (top left) Real part of the frequency (top right) Electric field direction (bottom left) The ratio between the electromagnetic and electrostatic electric field comonents (bottom right). The system parameter is $\gamma = 100$. The dominant mode $\Omega = 0.1i$ occurs at $Z_z = 0$

ables $\beta = \frac{P}{m\sqrt{1+\frac{P^2}{m^2c^2}}}$, $\gamma = \frac{1}{\sqrt{1-\beta^2}}$, $\mathbf{Z} = \frac{c\mathbf{k}}{\omega_p}$, $\Omega = \frac{\omega}{\omega_p}$, $\omega_p = \sqrt{\frac{4\pi q^2}{m}n}$. If the ISM particles reflect perfectly from the jet front, then the ISM centre of mass reference frame, both beams would move with the jet's Lorenrz factor, which is estimated at $\gamma = 100$.

Figure 9 exhibits the main features of the instability. The dom-

inant mode is perpendicular to the beam. The real part (and hence the pahse velocity) is zero (due to the symmetery of the system). The k space loci where the electromagnetic component of the beam maximises coincides with that of the dominant mode, which means that this instability generates magnetic fields.
By setting the dimensionless frequency to 0 in the dispersion equation, we obtain the stability condition

$$Z_z > \frac{\left(1-\beta^2\right)^{1/4}}{\beta} \tag{18}$$

To understand the reason for that, one must consider the problem from the beams' reference frame. A static wave with wavelength k_z in the lab refrence frame will seem as a wave with frequency $\frac{k_z c\beta}{\sqrt{1-\beta^2}}$ in the beams' refrence frame. The wave is stable if the frequency is greater than the plasma frequncy $\frac{k_z c\beta}{\sqrt{1-\beta^2}} > \omega_p'$. The plasma frequncy is proportional to the square root of the density. Since the density in the beam frame is lower by a factor of $\sqrt{1-\beta^2}$ from the density in the lab frame, the plasma frequency in the beam frame will be lower than that of the lab frame by a factor

of $\left(1-\beta^2\right)^{1/4}$. Hence the stability condition is

$$\frac{k_z c\beta}{\sqrt{1-\beta^2}} > \omega_p' = \frac{\omega_p}{\left(1-\beta^2\right)^{1/4}} \quad \Rightarrow \quad \frac{ck_z}{\omega_p} > \frac{\left(1-\beta^2\right)^{1/4}}{\beta} \tag{19}$$

Which is equivalent to the result we obtained from the dispersion equation [18]. In addition, by substituting $\Omega = 0$ into the expression for the ratio of the electric field components we obtain

$$\left(\frac{E_z}{E_x}\right)_{\Omega=0} = \frac{k_z}{k_x} \tag{20}$$

Which means that the instability stops when the electric field aligns with the wave vector. When that happens, $\mathbf{k} \times \mathbf{E} = 0$, so the magnetic field does not grow.

Another notable property of this scenario is that the fastest growing mode occurs at

$$Z_Z = \frac{\sqrt{\left(1-3\beta^2\right)\left(3-\beta^2\right)}}{2\sqrt{2}\beta\sqrt{1-\beta^2}} \tag{21}$$

Hence the mode is oblique when $\beta < \frac{1}{\sqrt{3}}$ and perpendicular to the beams when $\beta > \frac{1}{\sqrt{3}}$.

4.1.2 Cold Beams of different densities

In order to calculate instabilities in this scenario, we make two modification to the previous distribution function. The first (and obvious) is to change the density of one of the beams. This is achieved by multiplying one of the terms by a constant $0 < \alpha \leq 1$ (density ratio). After this modification, the electron beams have nonzero current, which means the protons must also move in order to cancel out the current. Hence, the second modification is a Lorentz transformation to a reference frame where the background is at rest. In that reference frame, the average momentum of the denser beam is

$$\alpha \frac{P}{m\sqrt{1+\frac{P^2}{m^2c^2}}} + \frac{P'}{m\sqrt{1+\frac{P'^2}{m^2c^2}}} = 0 \quad \Rightarrow \quad P' = \frac{\alpha P}{\sqrt{1+\frac{P^2}{m^2c^2}\left(1-\alpha^2\right)}} \tag{22}$$

Finally, the distribution function

$$f\left(\mathbf{p}\right) = \frac{1}{1+\alpha}\delta\left(p_x\right)\delta\left(p_y\right)\left[\alpha\delta\left(p_z - P\right) + \delta\left(p_z + \frac{\alpha P}{\sqrt{1+\frac{P^2}{m^2c^2}\left(1-\alpha^2\right)}}\right)\right] \tag{23}$$

The resulting dispersion equation is polynimal, so according to the fundamental theorem of algebra, the number of distict roots is bounded by the order of the polynomial. Moreover, there exist algorithms for finding all the roots [29] so the problem is numerically solvable. In presenting the results we used the same dimensionless variables as in the previous section. We used the arbitrary value $\alpha = 0.001$ to emphasize the different between this and the case of equal densities.

Figure 10 exhibits the main features of instabilities in this scenario. The wavevector of the dominant mode is at an acute angle with the beam direction. The real part is nonzero, and increases monotonically with Z_z (the graph can be misleading. closer inspection of the analytical solutions reveals that the relation between Z_Z and $\Re(\Omega)$ is more complicated). This means that the unstable modes not only grow but also drift, and since the dispersion relation is not linear, different modes drift at different velocities. The electrostatic component of the electric field of the dominant mode is much greater than the electromagnetic compo-

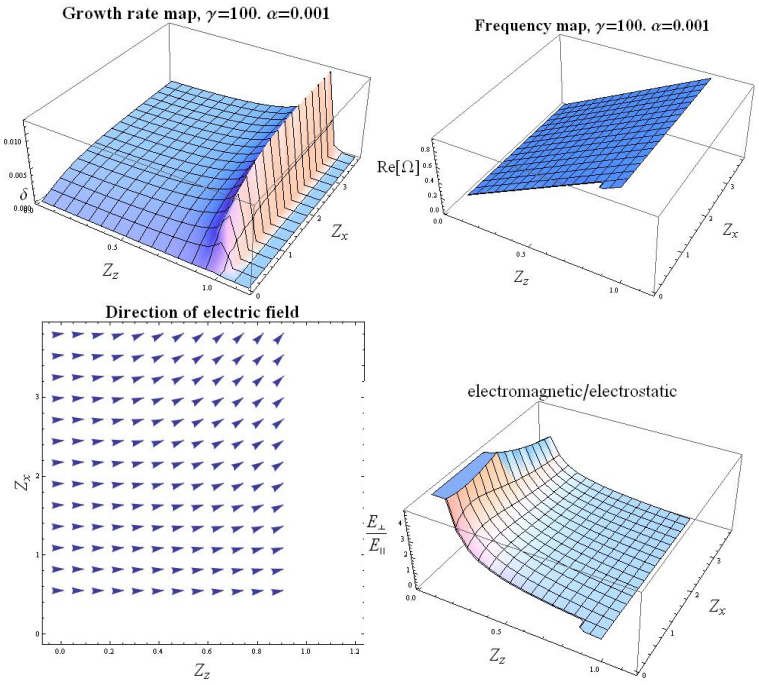

Figure 10: Imaginary part of the frequency (top left) Real part of the frequency (top right) Electric field direction (bottom left) The ratio between the electromagnetic and electrostatic electric field comonents (bottom right). The system parameters are $\gamma = 100$, $\alpha = 0.001$. The dominant mode $\Omega = 0.97 + 0.012i$ occurs at $Z_z = 0.97$.

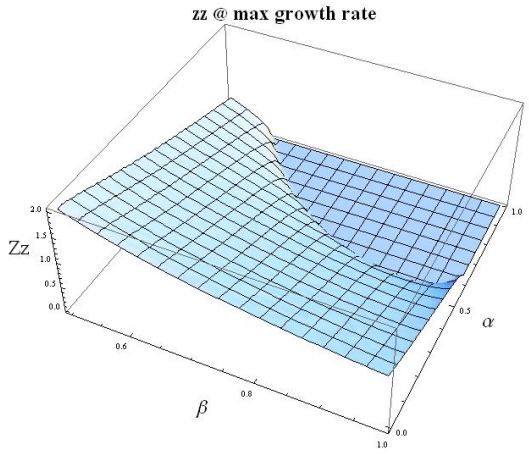

Figure 11: The value of the dimensionless wavevector component parallel corresponding to the dominant mode versus the system parameters

nent, which may suggest that this instability does not generate magnetic fields. Moreover, in the limit $k_x, k_z \to \infty$ equation 14 reduces to $E_x/E_z = k_x/k_z$, which implies that as the wavenumber increases, the instability becomes more electrostatic.

The dominant mode is not oblique in the entire parameter space, as can be deduced from figure 11.

The instability is perpendicular only for high values of α, β (in the above graph, the flat plateau at the upper right corner defines the parameter space area for which the instability is perpendicular). For other values of α, β, the instability is oblique. These results

are in agreement with PIC simulations [30].

4.1.3 Warm Beams of equal densities

The distribution function is given by

$$f(\mathbf{p}) = \frac{n}{\pi^{3/2} P_{th}^3} \exp\left[-\frac{p_x^2 + p_y^2}{P_{th}^2}\right] \left(\exp\left[-\frac{(p_z - P)^2}{P_{th}^2}\right] + \exp\left[-\frac{(p_z + P)^2}{P_{th}^2}\right]\right) \tag{24}$$

Where we used the following dimensionless variables $P_{th} = \rho mc$, $P = \frac{mc\beta}{\sqrt{1-\beta^2}}$, $\gamma = \frac{1}{\sqrt{1-\beta^2}}$. The ISM estimated temperature ranges from zero [37 to a few keVs [38]. These estimates limit ρ to the range $0.2 \geq \rho \geq 0$. We chose $\rho = 0.01$ as a representing value.

The instability condition for pure electromagnetic waves (i.e. waves that propagate perpendicular to the beam) is

$$Z_x < \frac{2}{\rho}\left(1 - \beta^2\right)^{1/4} \tag{25}$$

Or, in terms of dimensional variables

$$k_x < \frac{2m\omega_p}{P_{th}}\left(1 - \beta^2\right)^{1/4} = \sqrt{\frac{4\pi\left(2\gamma n\right)q^2}{T}} \tag{26}$$

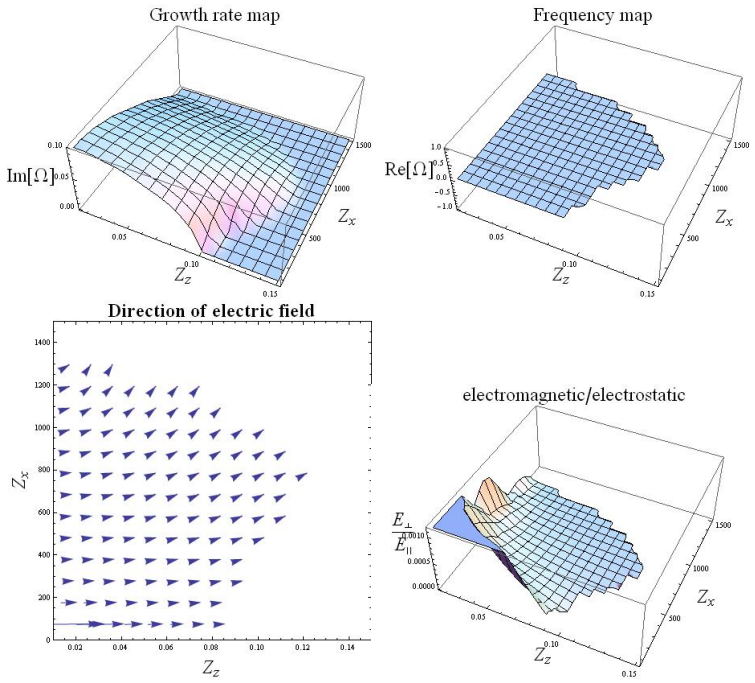

Figure 12: Imaginary part of the frequency (top left) Real part of the frequency (top right) Electric field direction (bottom left) The ratio between the electromagnetic and electrostatic electric field comonents (bottom right). The system parameters are $\gamma = 100$, $\rho = 0.01$. The dominant mode $\Omega = 0.1i$ occurs at $Z_z = 0$, $Z_x = 5$.

The expression on the rhs of the last equation is the inverse of the Debye length in the beams' rest frame. This condition simply means that when the filament is too thin, no Debye screening occurs and no energy is transferred to the plasma.

4.2 Background effect

In the previous section, we studied an instability that developed when between two beams in the presence of immobile background particles of opposite charge. In this section, we will study how the instability changes when the background is allowed to move. Moreover, we will assume that the background is composed solely of electrons, and the beams solely of protons, which are about 2000 times more massive.

Calculations in this sections purport to predict the second stage of the instability. We will ultimately wish to study two cases: symmetric and assymetric warm beams with hot background (we use the term warm to denote non - relativistic temperature and hot for ultrarelativistic temperature). The first corresponds to the

case where the ISM particles reflect perfecly from the jet front, while the second corresponds to imperfect reflection. We will not, however, approach the calculation immediately, but rather start with the simplest case and proceed gradualy by adding each effect at a time and studying them seperately. This will allow both to validate our calculations and gain insight on the effect of the initial conditions on the instabilities.

4.2.1 Cold beams, cold background

We assume that the proton distribution function is eq. 17 and the electrons is

$$f_e = n\delta\left(p_x\right)\delta\left(p_y\right)\delta\left(p_z\right)$$

Figure 13 exhibits the main features of instabilities in this scenario. The growth rate map reveals the two competing modes: the electromagnetic Weibel mode due to beam - beam interaction and the electrostatic Buneman mode due to beam - background interaction.

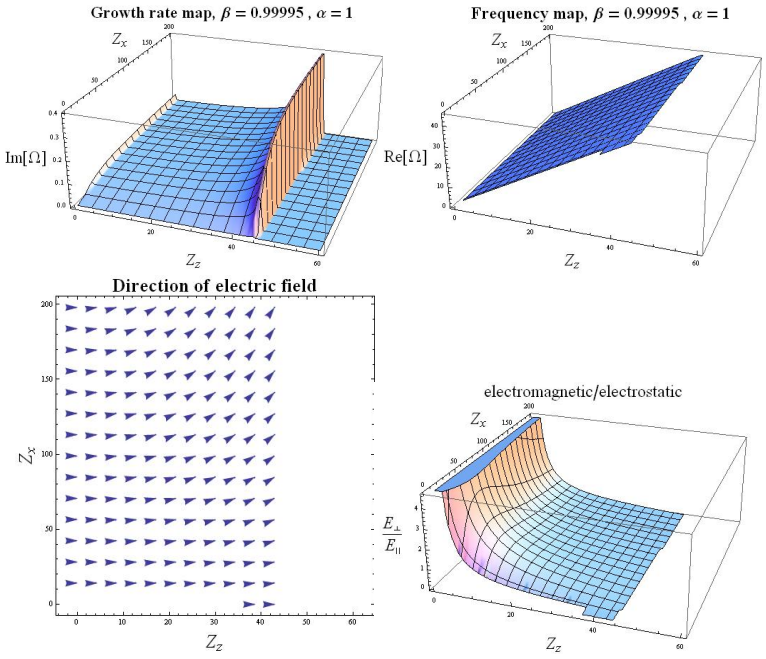

Figure 13: Imaginary part of the frequency (top left) Real part of the frequency (top right) Electric field direction (bottom left) The ratio between the electromagnetic and electrostatic electric field comonents (bottom right). The beams' parameter is $\gamma = 100$. The dominant mode $\Omega = 44.65 + 0.39i$ occurs at $Z_z = 45$

4.2.2 Cold beams with warm background

We assume that the protons are described by the distribution function in eq. 17 and the electrons are described by

$$f_e = \frac{n}{\pi^{3/2} P_{th}^3} \exp\left[-\frac{p_x^2 + p_y^2 + p_z^2}{P_{th}^2}\right] \tag{27}$$

We also assume that the thermal energy is neglibile in comparison to the electrons rest mass (i.e. non - reletivistic case). This distribution is charaterised by a single variable - P_{th}, which is proportional to the square root of the temperature. In presenting the results we will rather use the dimensionless variable $p_{th} = \rho m_e c$. As the temperature increases, the electrostatic mode stabilises, as can be seen in figure 14. Therefore, at low temperatures, the Buneman mode dominates, while at higher temperatures it becomes comparable with the Weibel mode. A qualitative description for this phenomenon was given in section 4.1.3.

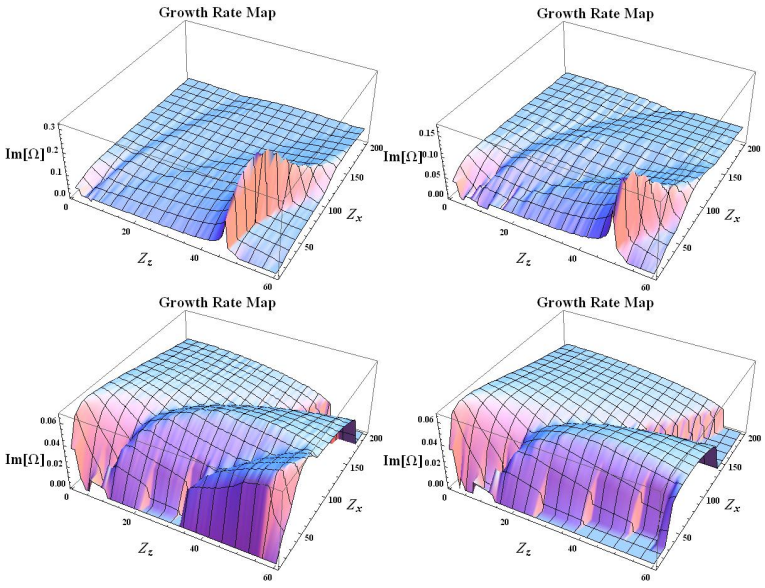

Figure 14: Growth rate maps for two counterstreaming symmetric cold beams with γ=100 at different background temperatures: $\rho = 0.2$ (top left) $\rho = 0.3$ (top right) $\rho = 0.4$ (bottom left) $\rho = 0.5$ (bottom right)

4.2.3 Warm beams of equal densities, hot background

We assume that the proton beams have non relativistic thermal energy, so they are described by drifting Maxwellian distribution-seq. 24. The electrons are assumed to to have ultrarelativistic temperature, so they are described by a relativistic distribution function for massless particles

$$f_e = \frac{n}{8\pi P_{th}^3} \exp\left[-\frac{\sqrt{p_x^2 + p_y^2 + p_z^2}}{P_{th}}\right] \tag{28}$$

P_{th} is proportional to the temperature. In the limit $P_{th,bg} \to \infty$, the system behaves as though the background is immobile. The reason is that the effective mass of the particles increases with the temperature, and hence the deviation from the unpertrubed trajectory decreases, so the instability weakens. From figure 15 we can see that even in ultrarelativistic temperatures, the Buneman mode still survives, and is even slightly stronger the Weibel mode. As the background temperature increases the Buneman mode decays and drifts towards the Z_x (i.e. its maximum occurs at lower Z_z). It vanishes/merges with the Weibel mode at a temperature equivalent to an order of magnitude of 10^5 times the electron rest mass energy. This greatly exceeds the most optimistic estimate on the kinetic energy of the jet, so the Buneman instability should occur in the second stage of every GRB afterglow.

According to assessment of the electron cooling rate [41,40], the ratio between the thermal energy of the elecrons after thermalisation and their initial kinetic energy lies in the range $0.1 < \varepsilon_e < 0.3$. We chose $\varepsilon_e = 0.15$ as a representing value, and since we assume that the initial electron energy is $\gamma = 15$, their temperature would

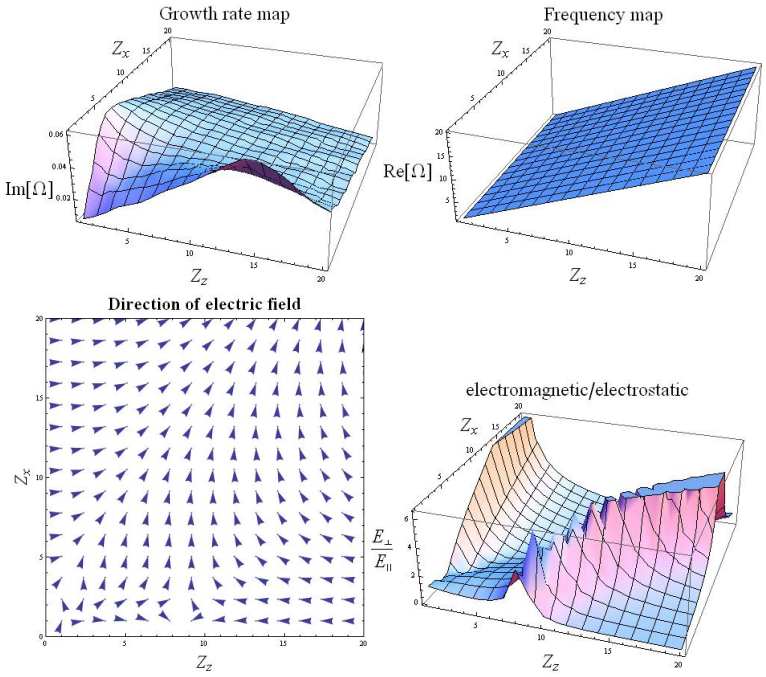

Figure 15: Imaginary part of the frequency (top left) Real part of the frequency (top right) Electric field direction (bottom left) The ratio between the electromagnetic and electrostatic electric field comonents (bottom right). The beams' parameter is $\gamma = 100$, $\rho = 0.1$, and the background parameters $\rho = 15$. The dominant mode $\Omega = 14 + 0.07i$ occurs at $(Z_z, Z_x) = (0, 14)$

be $\rho_{th,bg} = \frac{kT}{m_e c^2} = 15$.

4.2.4 Warm beams of different densities, hot background

We assume the proton beams distribution is

$$f_p = \frac{1}{1+\alpha}\frac{1}{\pi^{3/2}P_{th}^3}\exp\left[-\frac{p_x^2+p_y^2}{P_{th}^2}\right]\left(\exp\left[-\frac{(p_z-P)^2}{P_{th}^2}\right]+\exp\left[-\frac{1}{P_{th}^2}\left(p_z+\frac{}{\sqrt{1+}\right.\right.\right. \tag{29}$$

and the electron background distribution function 28. As in the symmetric case, this scenario gives rise to the Weibel mode and the Buneman mode. The existence of the Weibel (figure 16) mode implies that magnetic fields will be generated, in contrast to the asymmetric case in the absence of background. We also expect that in the limit $P_{th,bg} \to \infty$, we will recover the results for the latter case. The Weible mode disappears when $\frac{P_{th,bg}}{m_e c}$ is of the order of a few hundreds. In principle, current limitations on the jet energy and electron cooling rate, the electrons may exceed this limit, but we should expect this phenomenon to occur in most GRB afterglows.

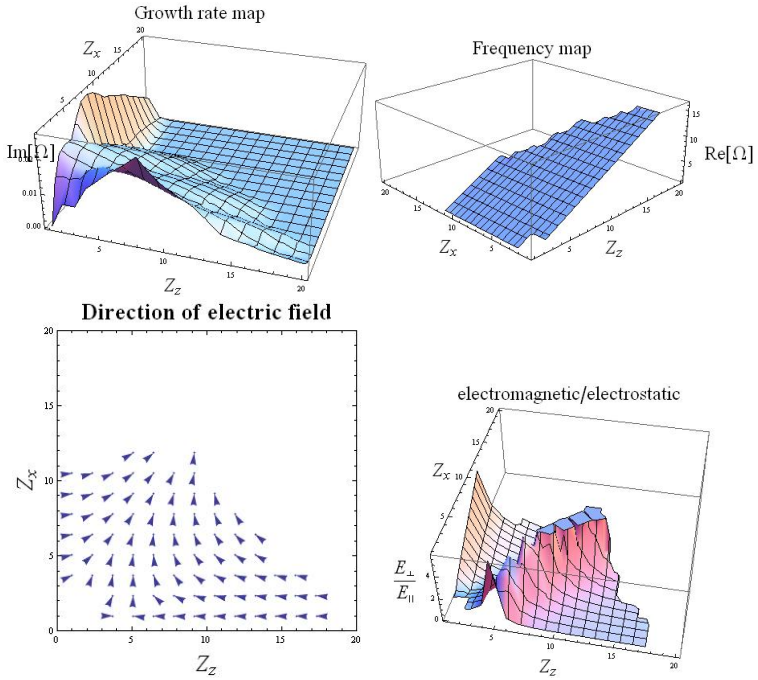

Figure 16: Imaginary part of the frequency (top left) Real part of the frequency (top right) Electric field direction (bottom left) The ratio between the electromagnetic and electrostatic electric field comonents (bottom right). The beams' parameter is $\gamma = 100$, $\rho = 0.1$, $\alpha = 0.1$, and the background parameters $\rho = 15$. The dominant mode $\Omega = 16 + 0.07i$ occurs at $(Z_z, Z_x) = (0, 16)$

5 Conclusions

In this section we summarize the results obtained in the previous sections and comment on their imlication to the two stage of the instability that developes in GRB afterglows.

5.1 First stage

We have seen that in case of a symmetric collision the Weibel instability dominates. If the beams' velocity exceeds a certain value (which is well below the ultrarelativistic limit) then the dominant mode is purely electromagnetic. If the ISM particles all reflect perfectly from the jet front, then the dominant mode would be the Weibel mode. However, if the reflection is not perfect (the particles either reflect with a lower speed or get absorbed in the jet) then the counter streaming profile would be asymmetric, so the dominant mode would be electrostatic and no magnetic fields will be generated.

5.2 Second stage

At very low background temperatures, the background - beam interaction overwhelms the beam - beam interaction. The dominant mode in these cases is electrostatic. When the background temperature rises, the background - beam interaction subsides, until it becomes comparable with the beam - beam interaction. This happens when the background temperature is of the order of tenths of the electron rest mass. For typical temperatures of thermalised electrons in GRB afterglows, an assuming symmetric reflection of ISM particles from the jet front, the system gives rise to two modes, one electromagnetic, and one electrostatic. however, a similar profile emerges even when the reflection is not perfect. Therefore, this phenomenon guarantees that magnetic fields will be generated, even if the assumption of perfect reflection does not hold. Thus, generation of magnetic field in GRB afterglows through the Weibel instability turns out to be more robust than previously realized. However, according to current limitation on GRB afterglow parameters, some afterglows can still avoid mag-

netic field generation by having both imperfect reflection (which prevents magnetic field generation in the first stage) and high electron thermalisation temperature (which prevents magnetic field generation in the second stage).

Appendices

A Dispersion equation for cold counter - streaming beams of equal densities

The dielectric tensor components are computed according to eq. 10

$$\varepsilon_{xx} = 1 - \frac{\omega_p^2}{\omega^2 \sqrt{\frac{P^2}{c^2 m^2} + 1}} \tag{30}$$

$$\varepsilon_{xz} = -\frac{c^4 k_x k_z m^2 P^2 \omega_p^2 \sqrt{\frac{P^2}{c^2 m^2} + 1}}{\omega^2 \left(c^2 m^2 + P^2\right) \left(c^2 \left(m^2 \omega^2 - k_z^2 P^2\right) + P^2 \omega^2\right)} \tag{31}$$

$$\varepsilon_{zz} = 1 - \frac{\omega_p^2 \left(k_x^2 P^2 + m^2 \omega^2\right) \left(c^2 \left(k_z^2 P^2 + m^2 \omega^2\right) + P^2 \omega^2\right)}{\sqrt{\frac{P^2}{c^2 m^2} + 1} \left(-c k_z^2 P^2 \omega + c m^2 \omega^3 + \frac{P^2 \omega^3}{c}\right)^2} \tag{32}$$

The dispersion equation is obtained by substituting these expressions into eq. 12. After multiplying by the lowest common denominator, the dispersion equation takes the form (in terms of the dimensionless variables)

$$\begin{aligned}
&\Omega^6 + \Omega^4 \left(-Z_x^2 - 2\beta^2 Z_z^2 - Z_z^2 + \sqrt{1-\beta^2}\beta^2 - 2\sqrt{1-\beta^2}\right) \\
&+\Omega^2 \left(2\beta^2 Z_x^2 Z_z^2 - \sqrt{1-\beta^2}\beta^2 Z_x^2 + \sqrt{1-\beta^2} Z_x^2 + \beta^4 Z_z^4\right. \\
&\left.+2\beta^2 Z_z^4 + \sqrt{1-\beta^2} Z_z^2 + \sqrt{1-\beta^2}\beta^4 Z_z^2 + \beta^4 - 2\beta^2 + 1\right) \\
&-\beta^4 Z_x^2 Z_z^4 + \sqrt{1-\beta^2}\beta^2 Z_x^2 Z_z^2 - \sqrt{1-\beta^2}\beta^4 Z_x^2 Z_z^2 - \beta^4 Z_x^2 + \beta^2 Z_x^2 \\
&+\beta^6 Z_z^2 - \beta^4 Z_z^6 - 2\beta^4 Z_z^2 + \sqrt{1-\beta^2}\beta^2 Z_z^4 + \beta^2 Z_z^2 - 2\sqrt{1-\beta^2}\beta^4 Z_z^4 = 0
\end{aligned} \tag{33}$$

References:

1. L. D. Landau, E. M. Lifshitz, *Statistical Physics, Part 1*, Pergamon Press. (1980)

2. D. Bohm & E. P. Gross, Phys. Rev. **75,** 1851 & 1864 (1949)

3. O. Buneman, Phys. Rev. 115, 503 (1959)

4. E. S. Weibel, Phys. Rev. Lett. **2**, 83 (1959)

5. B. Fried, Phys. Fluids **2**, 337 (1959)

6. S. A. Bludman, K. M. Watson & M. N. Rosenbluth, Phys. Fluids **3**, 747 (1960)

7. L. E. Thode, R. N. Sudan, Phys. Rev. Lett. 30, 732

8. F. Califano, F. Pegoraro, S. V. Bulanov & A. Mangeney, Phys. Rev. E, 57, 7048

9. G. A. Askar'yan, S. V. Bulanov, F. Pegoraro, A. M. Pukhov, JETP Lett. 60, 241 (1994)

10. P. H. Yoon & R. C. Davidson, Phys. Rev. A, **35**, 6 (1986)

11. A. Bret, M. C. Firpo & C. Deutsch, Phys. Rev. Lett. 94, 115002 (2005)

12. F. Pegoraro, S. V. Bulanov, F. Califano & M. Lontano, Phys. Scr. Vol. T63, 262 (1996)

13. T. Piran, Rev. Mod. Phys. 76, 1143 (2005)

14. T. Piran, Phys. Rept. 314, 575 (1999)

15. M. V. Medvedev, ApJ, 540, 704 (2000)

16. G. B. Rybicki & A. P. Lightman, *Radiative Processes in Astrophysics,* John Wiley and Sons (1979)

17. M. V. Medvedev, D. Lazzati, B. C. Morsony & J. C. Workman, ApJ 666, 339 (2007)

18. A. Achterberg, J. Wiersma, A&A, 478, 18 (2007)

19. A. Achterberg, J. Wiersma, A&A, 478, 19 (2007)

20. Y. Lyubarski, D. Eichler, ApJ 647, 1250 (2006)

21. M. Tabak, J. Hammer, M. E. Glinsky, W. L. Kruer, S. C.

Wilks, J. Woodworth, E. M. Campbell, M. D. Perry & R. J. Mason, Phys. Plasmas, 1, 1626 (1994)

22. M. E. Dieckmann, L. O'C Drury & P. K. Shukla, New J. phys., 8, 40 (2006)

23. J .T. Frederiksen, C. B. Hededal, T. Haugbolle & A. Nordlund, ApJ 608, L13 (2004)

24. J. M. Dawson, Rev. Mod. Phys. 55, 2 (1983)

25. M. Medvedev and A. Loeb, Astrophys. J. **526**, 697 (1999)

26. R. A. Fonesca, L. O. Silva, J. W. Tonge, W. B. Mori, J. M. Dawson, Phys. Plasmas, 10, 1979 (2003)

27. A. Bret, M. C. Firpo, C. Deutsch, Phys. Rev. E, 70, 046401 (2004)

28. T. P. Wright, G. R. Hadley, Phys. Rev. A, 12, 2 (1975)

29. W. H. Press, S. A. Teukolsky, W. T. Vetterling & B. P. Flannery, *Numerical recipes in Fortran,* Cambridge university press (1994)

30. M. E. Dieckmann, J. T. Frederiksen, A. Bret & P. K. Shukla, phys. plasmas 13, 112110 (2006)

31. A. Shemi & T. Piran, ApJ. 365, L55 (1990)

32. B. Paczynski, ApJ. 363, 218 (1990)

33. A. Bret, L. Gremillet, D. Benisti & E. Lefebvre, Phys. Rev. Lett. 100, 205008 (2008)

34. A. Dar, A. De Rujula, arXiv: astro-ph/0102115 (2008)

35. E. Liang, B. Zhang, B. Zhang, Z. G. Dai, arXiv: atro-ph/0606565 (2006)

36. A. Pe'er, arXiv: 0809.0903 (2008)

37. A. Gruzinov, E. Waxman, ApJ 511, 852 (1999)

38. A. J. Marle, N. Langer, A. Achterberg, G. Garcia - Segura, arXiv: astro-ph/0611812 (2006)

39. A. Panaitescu, P. Kumar, Apj, 571, 779 (2002)

40. S. A. Yost, F. Harris, R. Sari & D. A. Frail, ApJ 597, 459 (2003)

41. R. A. M. J. Galama & T. J. Wijers, ApJ 523, 177 (1999)

42. A. Bret, ApJ 699, 990 (2009)

43. L. Gremillet, D. Benisti, E. Lefebvre & A. Bret, Phys. Plasmas 14, 040704 (2007)